Optimizing the Focusing Performance of Non-Ideal Cell-Free mMIMO Using Genetic Algorithm for Indoor Scenario

Ke Shen, Siavash Safapourhajari, *Member, IEEE*, Toon De Pessemier, Luc Martens, *Member, IEEE*, Wout Joseph, *Senior Member, IEEE*, and Yang Miao, *Member, IEEE*

Abstract—This paper proposes a genetic algorithm (GA) combined with ray tracer to generate a cell-free topology of massive MIMO (mMIMO) for the optimal focusing performance serving multiple users. The realistic hardware impairment, for instance the non-ideal power amplifier, is taken into account of the system modeling and topology optimization. To the best of our knowledge, this is the first attempt to apply GA in optimizing the hardware-impaired multi-user cell-free mMIMO. Although the demonstrated numerical analysis is for indoor scenario, the proposed approach is transferable for generic scenarios. In GA, the base station (BS) antennas' placement is encoded with an adjusted binary matrix representation, which is straightforward for the subsequent genetic operations. The explored candidates by GA can evolve beyond the parents, where the fitness of individuals is evaluated dynamically via a ray tracer radio channel simulator. Compared to the traditional GA, our proposed GA can find better solutions with a faster convergence speed. The algorithm provides near-optimal results in experiments, applicable to generic environment with multiple mobile users and different signal-to-interference-plus-noise ratios.

Index Terms—Cell-free massive MIMO, multi-user, focusing performance, radio propagation channel, ray tracer, genetic algorithm, antenna deployment, 5G, 6G.

I. INTRODUCTION

WE ARE in the era of beyond-5G and towards-6G [1], [2], where the mobile communication networks with even lower latency, higher spectral efficiency, and higher reliability are under research and development, to satisfy the immensely increased wireless data consumption via diverse applications and devices. The massive multiple-input multiple-output (mMIMO) radio system is one of the key features in the next generation evolution. A mMIMO system is the system with unconventionally many active antenna elements with a total number of M that can serve K user equipment (UE) $(M \gg K)$ in the same time-frequency resources [3]. The

ratio between M and K depends on the requirements of system performance, the propagation environment, etc. For sub-6 GHz, massive multi-antenna base station (BS) with 64 or 128 antennas appeared as commercial products. For millimeter-wave (mmWave) frequencies, systems equipping more than 128 antennas are foreseen. In perspective of functionality, a mMIMO system can simultaneously transmit multiple independent streams where each experiences unique and independent propagation. Therefore, the spectral efficiency increases as a spatial multiplexing gain. It can also transmit coherent signals to antennas so that the signals add up coherently towards the target user then the signal-to-noise ratio (SNR) increases as a beamforming gain [4]. A mMIMO system is a solution for multi-user (MU) scenarios exploiting simultaneously the spatial multiplexing gain and the adaptive beamforming gain.

One of the important properties of the mMIMO system is the spatial resolution, depending on the aperture size, allocated radiating elements, allocated band, signal processing, and the BS-UE topology [5]. Typical types of topology include the co-located, the distributed, and the cell-free [6]–[8]. For the co-located topology, the BS array aperture is configured with the closely spaced (either with a uniform spacing of half-wavelength, or non-uniform spacing) antennas with specific geometry, and there is low requirement for the backhaul network. For the split topology, also called the distributed array, the BS array aperture is split and distributed in separated locations, and a cooperative backhaul network is necessary. For the cell-free topology, also known as "radio stripes", each user is essentially surrounded by the BS antennas, which differs from the traditional commercial network deployment that each BS is surrounded by users. It requires large-scale cooperative backhaul network. In this paper, our interest lies in the cell-free topology for MU-mMIMO.

The effectiveness and efficiency of a MU-mMIMO system are evaluated by its focusing performance to the active users. Given an explicit mMIMO topology, the intrinsic challenge posing between the BS and UE is the dispersive and directive radio propagation channel. The knowledge of the site-specific mMIMO radio channel, namely, the multipath, physical mechanism, delay spread, angular spread, coherent bandwidth, coherent time, etc., is crucial in order to evaluate the focusing performances of BS over the spread of mobile UE. The focusing performance incorporates the radio channel

condition with the tuning of precoding techniques, which typically include the maximum ratio transmission (MRT), the regularized zero forcing (ZF) and the minimum mean squared error (MMSE) [9]. Nevertheless, the impacts of 1) the mMIMO topology, 2) the MU effect including mobility, and 3) the propagation environment and mechanism, on the system focusing performance, should be understood as a whole in practical settings including the system imperfection or hardware impairment. Furthermore, these performance analysis incorporating practical factors should be able to offer hints for the optimal deployment. The mMIMO topology should be optimized in a smart way given the generic MU mobility, practical system imperfection and impairment, as well as realistic propagation channel condition.

In this paper, we propose to use a genetic algorithm (GA) combined with a ray tracing (RT) channel simulator to generate the optimal cell-free mMIMO topology serving MU in mobility. To conduct a realistic investigation, we incorporate the effect of the non-ideal hardware (HW) in the system model and GA, which has not yet been discussed in relevant earlier works. The 3D RT tool used in this paper can simulate various indoor and outdoor scenarios and has been validated in various literature [10]–[15]. We focus on the indoor scenario mainly due to the fact that we can better demonstrate the distributions of BS and UE antennas in a confined environment.

GA belongs to the broader class of the evolutionary algorithms (EA) inspired by the biological evolution: it encodes candidate solutions using chromosomes and provides a fitness function determining their qualities [16]. Over iterations, crossover and mutation are performed to generate new chromosomes, and selection is effectuated to preserve good chromosomes. So far, GA has been applied in MIMO technologies particularly for: the antenna array configuration design for MIMO BS [17] and MIMO UE [18], the array antenna selection [19], the MIMO Orthogonal Frequency Division Modulation (OFDM) resource allocation [20], the mmWave sparse channel estimation [21], and the network-level stochastic multi-objective optimization tasks [22]. GA is also used in [23] for a comparison with a gravitational search algorithm (GSA) to achieve the selection of the optimal transmit antennas maximizing both capacity and energy efficiency, but the implementation details are not given. Our earlier work [4] has proposed a GA for optimizing the cell-free mMIMO topology in a confined room, without considering the realistic MU mobility/dynamics nor the radio frequency (RF) hardware impairments.

In practice, different components of a transceiver distort the desired radio signal. The non-ideal power amplifier, the IQ imbalance in mixers and the phase noise are a few examples of non-ideal effects in transceivers. The effects of non-ideal hardware can be partially compensated using signal processing algorithms. Nevertheless, there will always be a residual impairment distorting the transmitted/received signal [24], [25]. To achieve a realistic system level performance analysis, these residual impairments should be taken into account. High level models of hardware impairments has been widely used in the literature for calculating capacity bounds and performance evaluation. A common method to model hardware impairments

is using an additive distortion term with a power proportional to the input signal power [24], [26]. A higher power of the distortion noise corresponds to a hardware with lower cost and lower quality. Measurements have shown that this tractable model provides an accurate description for the residual hardware impairments in RF transceivers [25]. This model can also be analytically motivated using a Bussgang decomposition as shown in [27] and has been extensively used to obtain the capacity bounds for MIMO and mMIMO systems.

Deploying a large number of access points in cell-free mMIMO leads to a considerable hardware cost. Therefore, it is interesting to investigate the effect of low quality (and low cost) hardware on the achievable performance. This has motivated recent research on the performance of cell-free mMIMO in the presence of hardware impairments [28]–[33] where the additive distortion noise model is used. In [28], the capacity bounds assuming maximum ratio combining/transmission are calculated for hardware impairments and a power control algorithm is proposed. The uplink capacity of cell-free mMIMO with four types of receiver cooperation and RF impairment is investigated in [29]. Furthermore, the effect of residual RF impairments on cell-free mMIMO has been studied while considering channel impairments [30], limited front-haul capacity [31], low resolution analogue digital conversions [32] and secrecy performance [33]. Similar to [24], [26], [28], in this work, the additive distortion noise is used to model the effect of residual hardware impairment on the achievable rates while optimizing topology using GA.

The contributions of this paper are threefolds:

- A system model incorporating non-ideal hardware is applied for cell-free mMIMO topology optimization in indoor scenarios. Simulation results show that the optimized deployment differs with the ideal and non-ideal hardware conditions. A genetic algorithm is proposed to optimize the cell-free mMIMO topology. Apart from the problem specific encoding, we introduce customized designs (warm-start strategy, selection policy, and elitism) to accelerate the convergence speed and to prevent the premature convergence.

- Using a ray tracer simulator, experiments from static to mobile UEs are performed with both ideal and non-ideal HW. Simulations mimicking the reality show the general applicability of the proposed algorithm and the corresponding workflow. The results also show the distinct optimization results for ideal and non-ideal hardware conditions, as well as the converged focusing performance with the increase of the ratio between the number of BS antennas and the number of UEs.

The remainder of this paper is organized as follows. Section II introduces the system model. Section III introduces the customized GA for this MU-mMIMO topology optimization problem. Section IV analyzes the numerical examples, and Section V concludes the paper.

II. SYSTEM MODEL AND FOCUSING PERFORMANCE

A. Cell-Free mMIMO Topology for Indoor Scenarios

There are two development directions for the mobile communication networks: one towards the higher mmWave or

THz frequency bands, hence larger available bandwidth and higher transmission data rates; the other towards the massive or even ultra mMIMO deployments for more consistent data rates. The cell-free mMIMO topology aims at providing an almost-uniformly good service quality for users everywhere [6] without the coverage dead zones, as well as an extreme spatial multiplexing using the physically large array apertures. Ideally, there is no division of cells, but just the spread out of access points: a massive number of distributed BS antennas. In this topology, each user is served by all the antennas in its occupancy area of influence, so that the user-centric clustering is formed to reinforce channel hardening [8], [34]. The cell-free topology requires a lot of backhaul signaling and massive deployment hence low-cost hardware is favorable. The cell-free mMIMO is feasible to implement not only outdoor but also in large indoor environments, e.g., the warehouse, factory, hospital, shopping mall, parking lot.

B. mMIMO System Model Incorporating Non-Ideal Hardware

Assume that the input signal, $x = \mathcal{CN}(0, p)$, passes through a nonlinear memoryless function $g(x)$. Then, the output $y = g(x)$ can be modeled as follows [27]:

$$y = \sqrt{\alpha}x + \eta, \qquad (1)$$

where α is a value $0 < \alpha < 1$ determining the portion of the power of x which is transferred to the output without distortion, while η is the additive distortion which is uncorrelated with x. It has been shown that the residual radio frequency impairments can be modelled using (1); in this case, it is assumed that $\eta \sim \mathcal{CN}(0, (1-\alpha)p)$ where p is the input power. For a wireless transceiver $1 - \alpha$ is equal to the square of the Error Vector Magnitude (EVM): EVM$= \sqrt{1-\alpha}$ [26], [28]. The EVM is a common measure for evaluating the quality of transceivers, and according to the 3GPP Release 15 for BS and UE, an EVM in the range of $[0.08, 0.175]$ is acceptable depending on the target modulation scheme, e.g., 256-Quadrature Amplitude Modulation (QAM) to Quadrature Phase Shift Keying (QPSK). This range of EVM corresponds to $0.97 < \alpha < 0.99$, where a larger α means that more expensive hardware is required. In massive MIMO applications, α values lower than 0.99 are more interesting as they decrease the cost of hardware [24], [28].

We use the above mentioned model for a transmitter t and receiver r, and use α_t and α_r to denote the quality factors in the transmitter and receiver, respectively. In this work the optimization is performed considering the downlink (DL) efficiency. Thus, for the access points (APs), the transmitter nonlinearity α_t is considered, whereas for UE, the receiver nonlinearity is of interest so α_r is used for the UEs. It is assumed that all UEs and all APs have the same quality; therefore, the same values are considered for α_r for all UEs and the same α_t for all APs.

To derive the system model in the presence of hardware impairments, assume that $s = [s_1, \ldots, s_K]^T$ is the desired signal for K users. Then, $s' \in \mathbb{C}^{K \times 1}$ upon power allocation

is obtained as follows:

$$\mathbf{s}' = \sqrt{\mathbf{P}}s = [\sqrt{p_1}s_1, \ldots, \sqrt{p_K}s_K]^T, \qquad (2)$$

where p_k $(k = 1, \ldots, K)$ is downlink power allocated to user k. Using a precoding matrix $\mathbf{W} \in \mathbb{C}^{M \times K}$ the desired transmitted signal is derived as follows:

$$\mathbf{x} = \mathbf{W}\mathbf{s}', \qquad (3)$$

where $\mathbf{x} = [x_1, \ldots, x_M]^T \in \mathbb{C}^{M \times 1}$, and for each AP $x_m \sim \mathcal{CN}(0, \sigma_m^2)$ and σ_m^2 is achieved as follows ($|s_i|^2 = 1$):

$$\sigma_m^2 = \sum_{i=1}^{K} |w_{m,i}|^2 p_i. \qquad (4)$$

When $\mathbf{x}$ is passed through a non-ideal transmitter, the transmitted signal is:

$$\mathbf{x}_{TX} = \sqrt{\alpha_t}\mathbf{x} + \boldsymbol{\eta}^t, \qquad (5)$$

where α_t is the aforementioned HW quality factor for APs and $\boldsymbol{\eta}^t = [\eta_1^t, \ldots, \eta_M^t]^T$ is the vector of additive distortion at the transmitter of M APs. For the mth AP, $\eta_m^t \sim \mathcal{CN}\left(0, (1-\alpha_t)\sigma_m^2\right)$.

The transmitted signal $\mathbf{x}_{TX}$ is received by each user with a non-ideal receiver. Thus, the received signal per UE can be modelled adopting (1):

$$y_k = \sqrt{\alpha_r}\mathbf{h}_k\mathbf{x}_{TX} + \eta_k^r + n_k, \qquad (6)$$

where α_r is the aforementioned HW quality factor for UEs, $\mathbf{h}_k = [h_{k,1}, \ldots, h_{k,M}] \in \mathbb{C}^{1 \times M}$ includes the channel coefficients from M APs to the kth user (the kth row of the channel matrix $H \in \mathbb{C}^{K \times M}$), and $n_k \sim \mathcal{CN}(0, \sigma^2)$ is the additive white Gaussian noise (AWGN) noise. $\eta_k^r \sim \mathcal{CN}(0, (1-\alpha_r)P_k^{RX})$ is the additive distortion at the receiver of the kth UE where P_k^{RX} is the power of the received signal ($\mathbf{h}_k\mathbf{x}_{TX}$) at the kth user. Based on (2)-(5), $\mathbf{h}_k\mathbf{x}_{TX}$ can be written as follows:

$$\mathbf{h}_k\mathbf{x}_{TX} = \sum_{i=1}^{K} \sqrt{\alpha_t}\mathbf{h}_k\mathbf{w}_i\sqrt{p_i}s_i + \mathbf{h}_k\boldsymbol{\eta}^t, \qquad (7)$$

where $\mathbf{w}_i$ is the ith column of the precoding matrix $\mathbf{W}$. Since $\eta_m^t \sim \mathcal{CN}(0, (1-\alpha_t)\sigma_m^2)$, P_k^{RX} can be achieved as follows:

$$P_k^{RX} = \sum_{i=1}^{K} \alpha_t |\mathbf{h}_k\mathbf{w}_i|^2 p_i + \sum_{m=1}^{M} |h_{k,m}|^2 (1-\alpha_t)\sigma_m^2.$$

The expression for y_k can be further modified by substituting $\mathbf{x}_{TX}$ from (5) into (6) to write:

$$y_k = \sqrt{\alpha_r\alpha_t}\mathbf{h}_k\mathbf{x} + \sqrt{\alpha_r}\mathbf{h}_k\boldsymbol{\eta}^t + \eta_k^r + n_k. \qquad (8)$$

Separating the desired signal at the kth user, the following expression can be achieved:

$$y_k = \sqrt{\alpha_r\alpha_t}\mathbf{h}_k\mathbf{w}_k s_k' + \sqrt{\alpha_r\alpha_t}\sum_{i=1,i\neq k}^{K} \mathbf{h}_k\mathbf{w}_i s_i' \qquad (9)$$

$$+ \sqrt{\alpha_r}\mathbf{h}_k\boldsymbol{\eta}^t + \eta_k^r + n_k. \qquad (10)$$

The first and the second terms are the desired signal for the kth user and the interference from other users, respectively.

Therefore, the power of the desired signal at the kth user ($P_{S,k}$) and the power of the interference from other users ($P_{I,k}$) can be derived as follows.

$$P_{S,k} = \alpha_r \alpha_t |\mathbf{h}_k \mathbf{w}_k|^2 p_k, \tag{11}$$

$$P_{I,k} = \sum_{i=1, i\neq k}^{K} \alpha_r \alpha_t |\mathbf{h}_k \mathbf{w}_i|^2 p_i, \tag{12}$$

The third and the fourth terms in (10) are distortion terms resulting from RF impairments. Replacing values of $\boldsymbol{\eta}^t$ and η_k^r (see explanations for (5) and (6)), the overall power of these two terms, denoted by N_k^{HW}, and can be derived following the three steps below:

Step 1:

$$N_k^{HW} = \sum_{m=1}^{M} \alpha_r |h_{k,m}|^2 (1-\alpha_t)\sigma_m^2 + (1-\alpha_r)P_k^{RX}, \tag{13}$$

Step 2:

$$N_k^{HW} = \sum_{m=1}^{M} \alpha_r |h_{k,m}|^2 (1-\alpha_t)\sigma_m^2$$
$$+ (1-\alpha_r)\sum_{i=1}^{K} \alpha_t |\mathbf{h}_k \mathbf{w}_i|^2 p_i$$
$$+ (1-\alpha_r)\sum_{m=1}^{M} |h_{k,m}|^2 (1-\alpha_t)\sigma_m^2, \tag{14}$$

Step 3:

$$N_k^{HW} = (1-\alpha_r)\sum_{i=1}^{K} \alpha_t |\mathbf{h}_k \mathbf{w}_i|^2 p_i$$
$$+ \sum_{m=1}^{M} |h_{k,m}|^2 (1-\alpha_t)\sigma_m^2. \tag{15}$$

Replacing σ_m^2 with its value from (4), we have:

$$N_k^{HW} = (1-\alpha_r)\sum_{i=1}^{K} \alpha_t |\mathbf{h}_k \mathbf{w}_i|^2 p_i$$
$$+ \sum_{m=1}^{M} |h_{k,m}|^2 (1-\alpha_t)\sum_{i=1}^{K} |w_{m,i}|^2 p_i, \tag{16}$$

which finally leads to the following expression:

$$N_k^{HW} = (1-\alpha_r)\sum_{i=1}^{K} \alpha_t |\mathbf{h}_k \mathbf{w}_i|^2 p_i$$
$$+ (1-\alpha_t)\sum_{m=1}^{M} \sum_{i=1}^{K} |h_{k,m} w_{m,i}|^2 p_i. \tag{17}$$

From (10), (11), (12) and (17) and considering n_k power equal to σ^2, the Signal to Interference and Noise Ratio (SINR) for the kth user shown by $SINR_k$ is generated by:

$$SINR_k = \frac{\alpha_r \alpha_t |\mathbf{h}_k \mathbf{w}_k|^2 p_k}{\sum\limits_{i=1, i\neq k}^{K} \alpha_r \alpha_t |\mathbf{h}_k \mathbf{w}_i|^2 p_i + N_k^{HW} + \sigma^2}, \tag{18}$$

Till now, the system model with non-ideal effect has been completed. As was mentioned earlier in Section II.B and in

TABLE I
HARDWARE QUALITY FACTOR SPECIFICATION IN SYSTEM MODEL UNDER DIFFERENT CONDITIONS

Index	α_t	α_r	Comments
1	1	1	Both ideal
2	0.97	0.97	UE & AP worst case of 3gpp
3	0.95	0.95	
4	1	0.95	Only one side is non-ideal
5	0.95	1	
6	0.9	1	UE is ideal and different AP quality
7	0.8	1	
8	0.95	0.97	UE 3GPP wors case & different AP quality
9	0.9	0.97	
10	0.8	0.97	

the Introduction, to model different hardware quality in the transmitter (AP) and the receiver (UE), we can change the values of α_t and α_r, respectively. TABLE I shows a few examples of possible combinations of α_t and α_r. The quality factors are related to the actual hardware performance based on EVM. EVM for transceivers can include distortions resulting from a variety of sources such as power amplifier non-linearity and IQ imbalance. EVM is usually a figure of the residual distortion after the application of compensation methods (e.g., equalization, digital pre-distortion and so on [26]. The allowable range of EVM is determined by communication standards and the permitted value also depends on the used modulation schemes. The manufacturers should comply with these EVM values and ensure that their designed transceivers match the standard. Although the minimum value allowed by the current standard is 0.97 [35], it can be helpful to investigate how the focusing performance change for further decrease of the quality factors (lower quality hardware). This provides insights and measures for future technologies. That's why in [31], [32], [36] the α values are set to lower than 0.97 (which is the minimum value required for a QPSK system in [35]). For different parts of a system, e.g., power amplifier and receiver, the measurement setup for EVM may differ. In this work, we stick to a general use of EVM as a measure for hardware quality and hardware impairment model, simular to what was presented in [24]. We give examples of different values in TABLE I and how they can be interpreted. To demonstrate the performance of the optimization algorithm in a more realistic scenario, its performance for a pair of hardware non-ideality coefficients is presented. More information on EVM, and how it can be characterized for a system and examples of using it to demonstrate hardware quality can be found in [35], [37]–[41].

For a meaningful realistic applications and for the completeness of simulation results, the non-ideal scenario (both UE and AP have the worst hardware quality allowed by 3GPP that $\alpha_t = \alpha_r = 0.97$) is investigated in Section IV and compared with the ideal scenario.

C. Ideal mMIMO System Model

The ideal mMIMO system model without considering the non-ideal HW follows our earlier work in [4] - a specific case for condition No. 1 in Table I. The results will be demonstrated
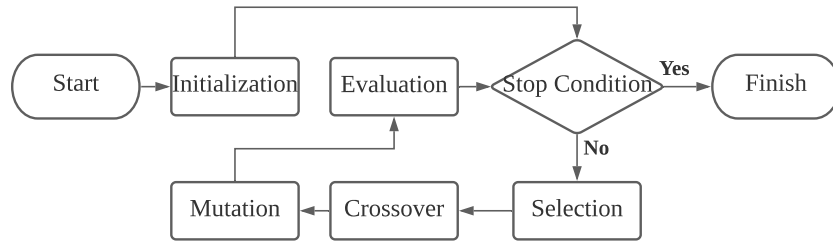
Fig. 1. Flowchart of the CGA.

in Section IV for comparison with the system performance with HW impairment.

III. GENETIC ALGORITHM CUSTOMIZED FOR MU-mMIMO TOPOLOGY OPTIMIZATION

In this paper, optimizing the cell-free mMIMO topology is considered as a combinatorial optimization problem, whose objective is to find combinations of BS antenna locations providing near-optimal focusing performances for a number of mobile UEs. Since BSs can be deployed anywhere in a confined environment, the design space of the problem is enormous and not tractable with exhaustive search. Because the focusing performance is correlated with setups of UE and BS (also the radio propagation environment), the objective space of the problem is unknown before planning. The GA is suitable for such fuzzy optimization problem because of its potential to optimize over iterations. With elitism selection [42], GA has an important characteristic that the final individuals in each generation would have equal or better fitness values than the starting individuals. Different from exact algorithms like mathematical programming, the proposed solution by GA is suboptimal (near-optimal) because the search progress could trap in local optima (the premature convergence). The advantage of applying GA is its ability to quickly find an acceptable solution. There are also some designs trying to prevent the premature convergence, including the warm-start [43] strategy to improve the quality or to increase the diversity of the initial population. Although the design of GA is problem-specific, in this section we present a customizable GA (CGA) with general applicability.

A. Encoding and the Fitness Function

In cell-free mMIMO, each UE is surrounded by enough BS antennas to ensure the uniformly good service quality. The focusing performance of a BS-UE typology is evaluated using the sum-rate capacity (an upper bound), i.e., substituting the SINR equation (18) for the systems with HW impairment, or, the SINR equation (7) in [4] for the ideal systems, to the capacity equation (9) in [4]. In the CGA, BS-UE typologies are encoded into mutable individuals (chromosomes) with customized representations of their locations.

Examples of encoding for different simulation scenarios are provided in Section IV. Multi-dimensional binary matrices are used to represent BS locations in the 3D coordinate system modeling the confined environment [4]. An applicable encoding should be time-efficient and easy to decode. With

such encoding, a BS-UE topology can easily convert into an individual in the CGA and vice versa. The fitness of an individual is defined as the focusing performance of the encoded BS-UE topology derived using the RT simulator.

B. Procedures of CGA

The flowchart of the CGA is shown in Fig. 1. Compared with the traditional genetic algorithm (TGA), the CGA has significant differences in the procedures. In this paper we introduce a *replacement strategy* as the warm-start strategy in its initialization stage: first the randomly generated individuals are ranked by their fitness values, afterwards the last $Q\%$ individuals are replaced by the best individual. Q is a customizable parameter since there is a threshold of individual variety and superiority. During the selection procedure, two individuals are further selected as parents for the following reproduction operations using the roulette-wheel selection [44]. The implementation details are given with the numerical experiments in Section IV.A.

In the reproduction stage, the crossover and mutation operations are carried out to generate offsprings. During the experiments in Section IV, single-point crossover [45] is applied to the parents with the binary matrix encoding by swapping parts of their genes, followed by a bit-flip mutation [46] on a random position. Figure 2 shows how parents are crossed over and mutated to generate new offsprings: the crossover gene is at index 3, therefore each of the offsprings will be a combination of the parents. The mutation positions of the offsprings are marked using color blue.

In the TGA without the elitism, the reproduction operations update the current generation by replacing the parent individuals with offspring individuals. The proposed CGA includes an elitism stage where the microbial elitism [47] strategy is used: the elitists are chosen between the (two selected) parents and the (two generated) offsprings, and preserved for the next generation.

Compared to the TGA, the CGA has the following benefits: the elitism stage prevents the destruction of the most fitting individuals during the evolution [48]. It also reduces the number of individuals chosen for the reproduction operations, since in the TGA many parent individuals are required to increase the possibility for generating better offsprings. The warm-start strategy also brings more high-quality individuals at the beginning of each iteration. These strategies can add selective pressure and improve convergence speed [49].

Fig. 2. Example of the reproduction operations.

Using the Bachmann–Landau notation (Big O notation), the time complexity of the CGA in the worst case can be calculated using the equation: $O(CGA) = P * O(fitness) + I * (O(Initialization) + O(Reproduction) + O(Elitism))$, where P is the population size, I is the number of iterations (generations). The complexity of different stages depends on the implementations. In the experiments we use the quicksort [50] for the stages where a sorting algorithm is required, therefore $O(Initialization)$ is $O(P^2)$. The reproduction (crossover and mutation) are triggered by the crossover rate pc and mutation rate pm. Their complexity depends on the encoding since the operations are performed on the chromosomes. In the elitism stage, the fitness of at most two new offspring need to be calculated. Using a RT simulator, time consumption for the fitness of an individual ($O(fitness)$) is comparatively much larger than other operations. Hence, $O(CGA)$ is deduced to $O(fitness)$.

IV. NUMERICAL EXPERIMENTS

In this section, the applicability and superiority of our proposed method over traditional approaches are demonstrated by numerical simulations and analysis in a confined environment (indoor but propagation condition transferable to outdoor scenarios), where the experimental results under different scenarios are compared. The following environment setups are applied for all scenarios: a confined room is represented using a cube with length, width and height as 5 meters. The frequency-dependent dielectric and conductivity properties of walls, ceiling and dryground follow the ITU-R recommendations [51]. There is no scattering from dryground, which is also impenetrable. The walls and ceiling are reflective and lossy bricks.

In the mMIMO system, the target frequency is 5.9 GHz with 200 MHz bandwidth. The base station antennas are half-wavelength vertical dipoles and each user is one single vertical dipole antenna as well. The line-of-sight (LOS) and the first order specular reflections (SRs) are captured in RT for the radio channel between base station antennas and user antennas. In all experiments multiple users (of number K) are randomly situated on the horizontal plane of $z = 1.6$ meters mimicking the human height. The BSs are assumed to be deployed on walls, whose number (M in total) and locations are decided by different approaches depicted in this section. To evaluate the focusing performance, we assume a constant SNR of 30 dB. We also use MMSE and equal power allocation, since the
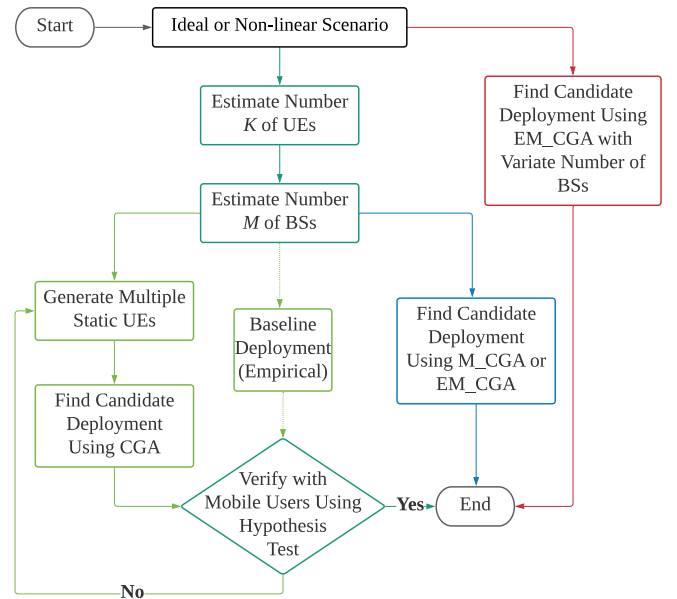

Fig. 3. Workflow of different experiments.

optimum power allocation and optimal precoding techniques are not the focus here in our paper.

Parameter settings of our proposed method are case-specific and will be presented with the numerical experiments in the next subsections. These settings ensure our methods to find an acceptable sub-optimal solution. All experiments are performed using Matlab R2017b on a normal PC with the Intel i7-7700 CPU. Workflows for different experiments are summarized in Fig. 3 to evaluate our proposed algorithm with different scenarios: the static UEs scenario follows the green routine; the mobile UEs scenario follows the blue routine (with shared steps in the static UEs scenario); the reality scenario follows the red routine.

A. Simulation With Static UEs

In the basic scenario shown in Fig. 4a, a snapshot of $K = 5$ UEs is denoted as ue_{5_0} (Note that ue_{K_i} denotes the ith snapshot of K UE locations) and their positions stay fixed during simulation. There are $M = 20$ BSs to deploy on the walls. It is worth mentioning that the M value is set small due to the rather simple environment and UE settings. As an empirical choice and easy to implement as a start, the baseline deployment is denoted as bs_{20_0} (Note that bs_{M_j} denotes jth topology of M BSs locations), where on each wall there are 5 BSs evenly located in the center as a row.

To propose a candidate topology for ue_{5_0} using the CGA, we keep part of the symmetrical assumption that the BSs are equally distributed on four walls (each wall has 5 BSs in this case) but their locations are random. Therefore, the encoding in CGA (and decoding is vise versa) is implemented as follows: each BS antenna location in the 3D Cartesian coordinate is represented using a binary matrix L, having 2 dimensions (2 rows) representing a 2D location on a plane (wall). The locating precision is determined by the length of L (number of columns). As an example, in this experiment L has 2 rows and 6 columns, with the locating precision of
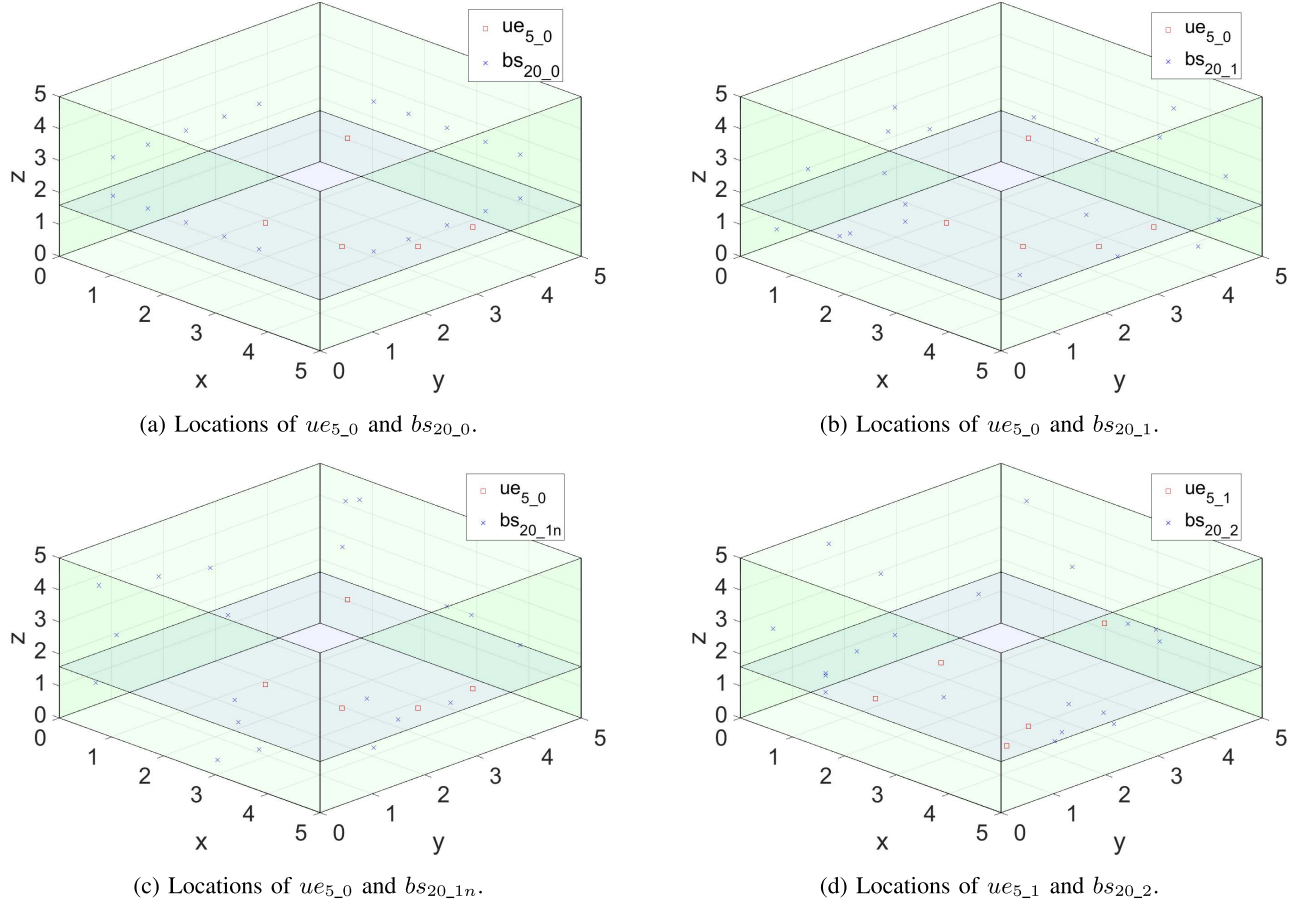
(a) Locations of ue_{5_0} and bs_{20_0}.

(b) Locations of ue_{5_0} and bs_{20_1}.

(c) Locations of ue_{5_0} and bs_{20_1n}.

(d) Locations of ue_{5_1} and bs_{20_2}.

Fig. 4. Locations of UEs and BSs in experiments with static UEs: (a) a static UE snapshot ue_{5_0} and the baseline deployment bs_{20_0}; (b) a static UE snapshot ue_{5_0} and the candidate deployment bs_{20_1} found by the CGA with the ideal scenario; (c) a static UE snapshot ue_{5_0} and the candidate deployment bs_{20_1n} found by the CGA with the non-ideal scenario; (d) a different static UE snapshot ue_{5_1} and the candidate deployment bs_{20_2} found by the CGA with the ideal scenario.

$5/(2^6) = 0.15625$ meters. The vector $[000000]$ indicates that the BS is 0.15625 meters to the boundary. As an example, the location of the BS antenna in the center of wall $y = 0$ is encoded with $L[1] = [011111]$ and $L[2] = [011111]$ indicating the relevant x-axis and z-axis values. A population is an array containing P instances of L, whose orders map the walls (e.g. $P[1..5]$ on wall $x = 0$, $P[6..10]$ on wall $y = 0$).

We compare the CGA and a traditional GA (TGA from [52]) with the same input ue_{5_0} and the same parameter settings. In both algorithms, the population size P is 4; the crossover rate pc is 0.85; the mutation rate pm is 0.15; the maximal iteration number I is 10. The Q for the replacement (warm-start) strategy in the initialization of the CGA is set to 50. For normal usage and for comparability with a standard GA, the 50% rate is recommended [47]. A common issue of the TGAs is that the algorithms are often trapped in the local optima, since the population tend to be too homogeneous during the evolution. To avoid such premature convergence, a fluctuating selection policy adapted from the roulette wheel selection is applied in the CGA: the probability p_i of an individual i to be selected in iteration k is defined using (19):

$$p_i = \frac{f_i}{\sum_{j=1}^{N} f_j}, \qquad (19)$$

where $f_i = |min_{j \in R} F_j + (max_{j \in R} F_j - min_{j \in R} F_j) \cdot \frac{I - k}{I - 1} - F_i| + \epsilon$, R is the set of all individuals in the current population, F_j is the fitness of individual j (focusing performance of the topology represented by j), and ϵ is a low positive value set as 0.01 to ensure a no-zero probability. With such selection policy, in the early generations (when k is small) the individuals with larger fitness values have a lower probability to be selected as parents than they should, and the individuals with lower fitness values have an increased probability to be chosen. In the final generations (when k is close to I), the individuals with higher fitness values have an increased selection probability to ensure the convergence of the algorithm.

The search trend of the two algorithms (distinguished by solid and hollow shapes) is provided in Fig. 5: Fig. 5a is with ideal UEs and BSs, while Fig. 5b is with non-ideal UEs and BSs (both α_r and α_t are the worst case of the 3GPP Release as 0.97). In these plots, the mean (marked with blue squares) and best (marked with green circles) fitness of individuals in each iteration are tracked.

For both ideal and non-ideal scenarios, in the first generation, the CGA has the better initial population than the TGA (having better mean and best fitness values) owing to the enabled warm-start strategy. In the following generations, the mean curves of both algorithms are rising since parents

TABLE II

VALIDATION OF BS TYPOLOGIES PROPOSED BY THE CGA WITH ue_{5_0} AS INPUT UNDER THE IDEAL AND NON-IDEAL SCENARIO

| BS	Scenario	Fitness (bit/s/Hz)
bs_{20_1}	**Ideal**	4.56
	Non-Ideal	2.04
bs_{20_1n}	Ideal	2.78
	Non-Ideal	3.32

are replaced by better offspring over iterations. The best individual in the final iteration is proposed by each algorithm as the solution to the BS-UE topology problem. For the ideal scenario, the CGA can find an individual (the decoded BS deployment is denoted as bs_{20_1} and visualized in Fig. 4b) with better fitness than the best individual found by TGA after 10 iterations, also requiring fewer iterations to converge (the mean and best curves of CGA remain unchanged since iteration 6 in Fig. 5a). The convergence of TGA is uncertain at iteration 10 since the mean curve is still approaching the best curve. For the non-ideal scenario where the fitness is generally lower than the ideal scenario, similar search trends are detected: the CGA has a faster convergence speed than the TGA and proposes a candidate with better fitness.

The proposed BS deployment by the CGA with the non-ideal scenario is denoted as bs_{20_1n} and visualized in Fig. 4c, where the positions of BSs differ significantly from those of bs_{20_1}. Summarized in Table II, the bold scenario names indicate where the CGA is used to generate the corresponding BS deployment, their performances are further evaluated with the ideal and non-ideal environment. The performance of the BS deployment bs_{20_1} (2.04 bit/s/Hz) can not outperform that of bs_{20_1n} (3.32 bit/s/Hz) under the non-ideal scenario; the performance of the BS deployment bs_{20_1n} (2.78 bit/s/Hz) can not outperform that of bs_{20_1} (4.56 bit/s/Hz) under the ideal scenario as well. Such phenomenon suggests that the CGA can find the best BS deployment for both scenarios, and such candidate deployment for one scenario is not transferable to the other. Therefore, the non-ideal scenario should be considered separately from the ideal scenario, and all the following experiments perform the comparisons between the two scenarios.

The sum-rate capacities of BS typologies in different experiments are summarized in Table III. In the previous basic simulation scenario, the deployment found by the CGA bs_{20_1} has better performance (4.56 versus 1.99 bit/s/Hz) than the baseline deployment bs_{20_0}. The search trend plots (in Fig. 5) also indicate that the CGA can find a converged and optimized solution with our parameter settings for both ideal and non-ideal scenarios. Such solution bs_{20_1} for the specific UE snapshot ue_{5_0} is further tested with 5 random UE snapshots, noted as $ue_{5\_[2..6]}$. The BS deployment bs_{20_1} can provide better performances than the baseline deployment bs_{20_0} for all testing UE snapshots, shown in Fig. 6. This phenomenon indicates that an optimized BS deployment found by the CGA for one UE snapshot can provide relatively good performances for others. It also implies that there might be an optimized BS deployment for all UE snapshots.
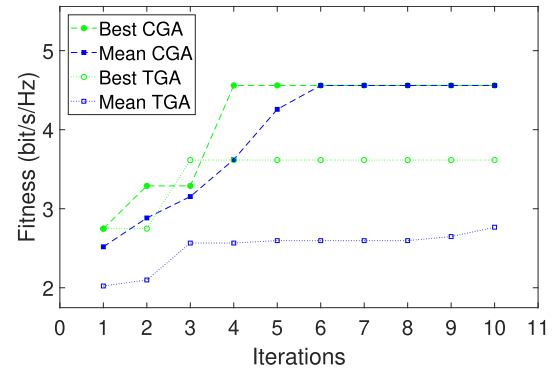
(a) Ideal: $\alpha_t = 1, \alpha_r = 1$.
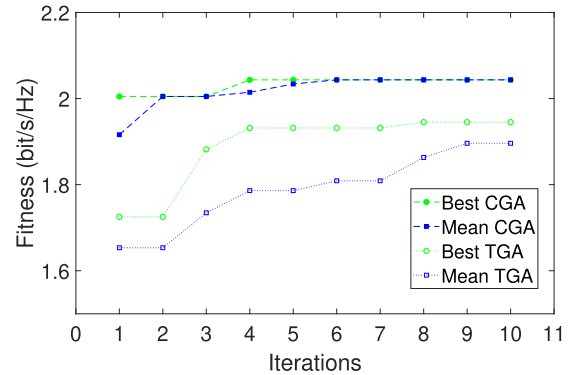
(b) Non-ideal: $\alpha_t = 0.97, \alpha_r = 0.97$.

Fig. 5. Search trend of the customized genetic algorithm (CGA) and the traditional genetic algorithm (TGA) for (a) the ideal and (b) non-ideal scenario.
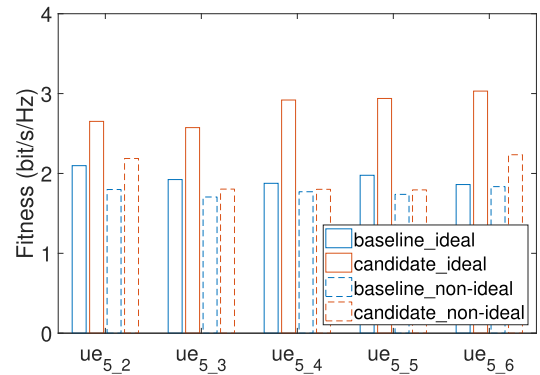

Fig. 6. Performances of the baseline deployment bs_{20_0} and the candidate deployment bs_{20_1} proposed by the CGA with 5 random UE snapshots for both the ideal and non-ideal scenario.

The positions of UEs and BSs are further investigated: in Fig. 4b, there is no obvious correlation between UEs and BSs locations in the room. On each wall, the BSs locations are neither related to each other. By applying the CGA with a static UE snapshot (e.g. ue_{5_0}), an optimized BS deployment (e.g. bs_{20_1}) is found for this snapshot, but might not be the best for other snapshots. As an example, for the snapshot ue_{5_2} the optimized BS deployment found by the CGA is bs_{20_2}. Therefore, the simulation scenario with static UEs is not sufficient for the generic BS topology problem "K mobile UEs with M BSs".

Scenario		UEs	BSs	Fitness (bit/s/Hz)
Ideal	Static	ue_{5_0}	bs_{20_0}	1.99
	Static	ue_{5_0}	bs_{20_1}	4.56
	Static	ue_{5_1}	bs_{20_2}	4.42
	Mobile	$m\_ue_{5\_5}$	bs_{20_3}	2.73 (avg)
	Mobile	$m\_ue_{5\_10}$	bs_{20_4}	3.12 (avg)
	Extra-mobile	$em\_ue_{5\_5}$	bs_{20_5}	2.52 (avg)
Non-ideal	Extra-mobile	$em\_ue_{5\_5}$	bs_{20_6n}	2.64 (avg)
	Extra-mobile	$em\_ue_{5\_5}$	bs_{20_7n}	2.50 (avg)
	Extra-mobile	$em\_ue_{5\_5}$	bs_{20_8n}	2.40 (avg)

B. Hypothesis Test With Multiple Static UEs

The previous section shows that the CGA can be applied to a static UE snapshot (ue_{K_i}) to obtain its optimized BS antenna deployment (bs_{M_j}), with both ideal and non-ideal scenarios. The corresponding performance (fitness) is denoted as $RT(ue_{K\_i}, bs_{M\_j})$. Since the mobile UEs scenario can be simulated with multiple static UEs snapshots (e.g. the Monte Carlo simulation, which is too time-consuming to apply in this case), hypothesis tests can be performed to compare the performances of BS deployments with mobile UEs. As an example, two BS topology deployments (denoted as bs_1 and bs_2) are achieved by the CGA with two static UE snapshots, their performances can further be verified with multiple snapshots imitating the mobile UE scenario, by conducting a two-sample t-test shown in Equation (20). The ith ($i \in \{1, 2\}$) population mean, sample size, sample mean, and sample standard deviation are denoted using μ_i, N_i, $\overline{x}_i$, and s_i. In such hypothesis test $N_1 = N_2 = N$, indicating bs_1 and bs_2 are verified using the same number of snapshots:

$$H_0 : \mu_1 \geq \mu_2$$
$$H_\alpha : \mu_1 < \mu_2$$
$$t = \frac{\overline{x}_1 - \overline{x}_2}{\sqrt{\frac{s_1^2}{N_1} + \frac{s_2^2}{N_2}}}. \qquad (20)$$

With a reasonable sample size N [53], by comparing the $t - statistics$ and by considering the $p - values$, we can accept or reject the null hypothesis H_0 that bs_1 can provide better performances for mobile UEs than bs_2. As a demonstration, we evaluate such hypothesis test on bs_{20_1} and bs_{20_2}, generated by CGA with ue_{5_0} and ue_{5_1} (ue_{5_1} and bs_{20_2} are visualized in Fig. 4d). From Table III, although $RT(ue_{5\_0}, bs_{20\_1})$ is better (4.56 versus 4.42 bit/s/Hz) than $RT(ue_{5\_1}, bs_{20\_2})$, with different static UE snapshots, bs_{20_1} might not have better performance than bs_{20_2} with mobile UEs.

In this experiment, different two-sample t-tests with different sample sizes (N) are conducted, for the simplification we only consider the ideal scenario. The Lilliefors test [54] is first applied to check the normality of all samples, as a prerequisite to a valid t-test. The normal probability plot [55] is used to visualize the chosen samples, plotting each data point and reference lines representing the theoretical normal distribution. In Fig. 7 the data points appear along the reference
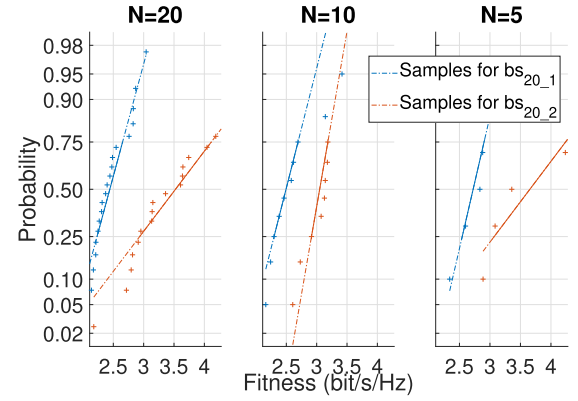

Fig. 7. Normal probability plots for ($N = 5$, $N = 10$, and $N = 20$) samples in the t-tests: the solid line connects the first and third quartiles, the dashed line extends the solid line to the ends.

TABLE IV
T-TEST RESULTS FOR bs_{20_1} AND bs_{20_2} PERFORMANCES WITH ($N = 5$, $N = 10$, AND $N = 20$) STATIC UE SNAPSHOTS (SAMPLES) SIMULATING MOBILE UEs

Class	Attributes	$N = 5$	$N = 10$	$N = 20$
bs_{20_1}	$\overline{x}_1$	2.73	2.60	2.45
	s_1	0.27	0.40	0.28
bs_{20_2}	$\overline{x}_2$	3.59	3.22	3.58
	s_2	0.68	0.51	0.82
Statistics	t	-2.62	-3.00	-5.80
	$p - value$	3.06×10^{-2}	7.60×10^{-3}	1.08×10^{-6}

lines, showing that the chosen samples approximate normal distributions. In Table IV the t-test results are summarized. With an increasing sample size N, all tests have negative $t - statistics$ and significant $p - value$ (< 0.05), indicating that the null hypotheses are rejected. Therefore, bs_{20_1} has worse performance than bs_{20_2} with mobile UEs.

With such verification method, a straightforward workflow for the generic BS deployment problem with mobile UEs is proposed as follows: start with several random static UE snapshots and generate the corresponding candidate BS deployments using the CGA. Further the performances of these BS deployments are verified with N static UE snapshots using hypothesis tests. The deployment having the best performance with mobile UEs is chosen as the final solution. This workflow has the following drawbacks: there are concerns that the starting UE snapshots are not adequately and randomly chosen, resulting in the neglect of candidate BS deployments for the further verification. Also, this method is time-intensive since it requires multiple executions of the CGA to generate candidate BS deployments, and multiple calls for the RT simulator to conduct the verification.

C. Simulation With Mobile UEs

Considering that random UE snapshots are chosen as inputs of the CGA and also samples for hypothesis tests, we can simplify the above mentioned workflow by integrating mobile UEs and verification processes into the CGA. However, the hypothesis tests were too complicated to be conducted among

the individuals for the rank of fitness in each iteration. Instead, we can barely compare the average performance of the individuals with mobile UEs according to the previous experiment. Suppose the CGA is started with N static UE snapshots (ue_{K_i}), the average performance of a BS deployment (bs_{M_j}) with these snapshots can be calculated using Equation (21):
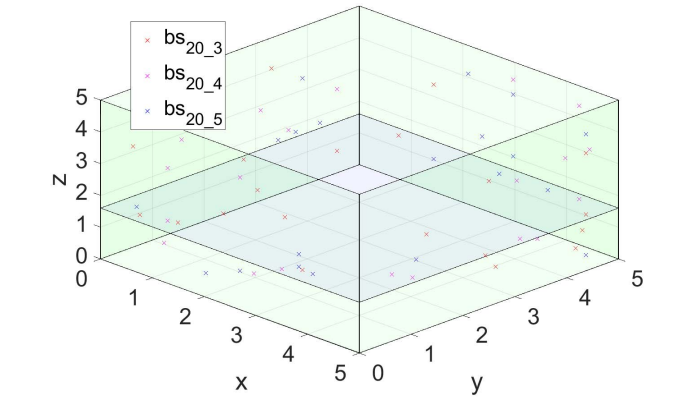
$$avg_j = \frac{\sum_{i=1}^{N} RT(ue_{K\_i}, bs_{M\_j})}{n}. \tag{21}$$

In the initialization stage, the algorithm (denoted as M_CGA) generates N snapshots of K static UEs (denoted as $m\_ue_{K\_N}$ in Table III). Over iterations, the fitness of an individual (encoding a BS deployment) is set as its average performance with such group of static UE snapshots. Table III provides the results of this method with $N = 5$ and $N = 10$ (Note that $K = 5$ in all experiments), where bs_{20_4} has better average performance (3.12 versus 2.73 bit/s/Hz) than bs_{20_3} with mobile UEs. Compared to the previous workflow, this integration method requires one execution of the M_CGA, but still multiple calls for the RT simulator. Each individual is verified with the same N static UE snapshots, requiring a relatively large sample size N for a convincing result. Also, the verification process of the preserved individual from the previous iteration is redundant in the subsequent iteration.
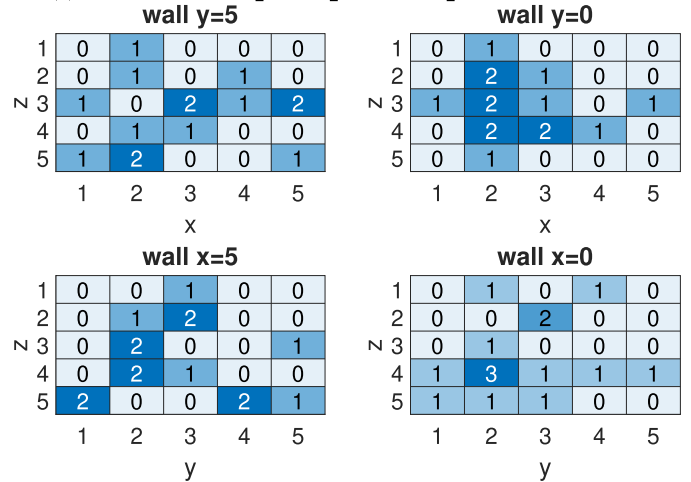
To avoid the aforementioned drawback, the algorithm (denoted as EM_CGA) applies another "extra-mobile" optimization strategy to generate N different snapshots of static UEs (denoted as $em\_ue_{K\_N}$ in Table III) in each iteration and rank the individuals by their average performances with such group of mobile UEs. With this strategy the preserved individuals are verified with different samples over iterations. Table III shows the performance of bs_{20_5} by applying this strategy with $N = 5$.

For the mobile user scenarios in Table III, although the performances of bs_{20_3}, bs_{20_4}, and bs_{20_5} are different, their locations are close to each other, visualized in Fig. 8a. On each wall the BSs positions of the three deployments are gathered into clusters varying over space. The heatmap plot in Fig. 8b, where each wall is equally divided into blocks of size $1 \times 1\ m$, counts the number of BS in each block and provides an intuitive view of the clusters. Fig. 8c is the heatmap of UEs on the user plane ($z = 1.6$). In total there are 65 UE scenarios, 5 for bs_{20_3} ($m\_ue_{5\_5}$), 10 for $bs20\_4$ ($m\_ue_{10\_5}$), and 50 for $bs20\_5$ ($em\_ue_{5\_5}$). Although there are fewer UEs in blocks against the walls because the UEs have a minimal separation distance from wall, in Fig. 8c all UEs are almost-equally distributed on the horizontal plane.
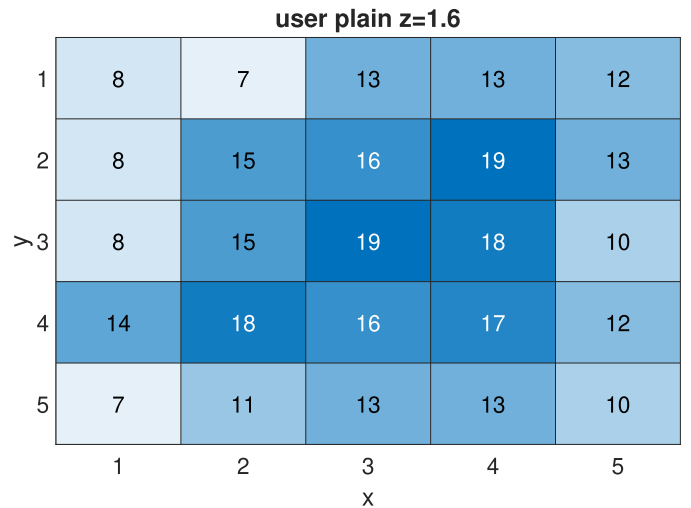
Note that the previous experiments are with the ideal scenario, we further verify the applicability of the proposed algorithm with the non-ideal scenario ($\alpha_t = 0.97$, $\alpha_r = 0.97$) with three "extra-mobile" experimental cases. Summarized in Table III, the corresponding candidate deployments bs_{20_6n}, bs_{20_7n}, and bs_{20_8n} are proposed by EM_CGA with their average performances. For these three deployments, the heatmaps of BSs on each wall are presented in Fig. 9a. Compared to the heatmaps with the ideal scenario in Fig. 8b, the BSs clusters are more obvious. The heatmap of UEs (in total there are 150 UE scenarios verified during iterations to

(a) Locations of bs_{20_3}, bs_{20_4}, and bs_{20_5} with mobile UEs.

wall y=5

N \ x	1	2	3	4	5
1	0	1	0	0	0
2	0	1	0	1	0
3	1	0	2	1	2
4	0	1	1	0	0
5	1	2	0	0	1

wall y=0

N \ x	1	2	3	4	5
1	0	1	0	0	0
2	0	2	1	0	0
3	1	2	1	0	1
4	0	2	2	1	0
5	0	1	0	0	0

wall x=5

N \ y	1	2	3	4	5
1	0	0	1	0	0
2	0	1	2	0	0
3	0	2	0	0	1
4	0	2	1	0	0
5	2	0	0	2	1

wall x=0

N \ y	1	2	3	4	5
1	0	1	0	1	0
2	0	0	2	0	0
3	0	1	0	0	0
4	1	3	1	1	1
5	1	1	1	0	0

(b) Heatmap of BSs on each wall for bs_{20_3}, bs_{20_4}, and bs_{20_5}.

user plain z=1.6

| y \ x	1	2	3	4	5
1	8	7	13	13	12
2	8	15	16	19	13
3	8	15	19	18	10
4	14	18	16	17	12
5	7	11	13	13	10

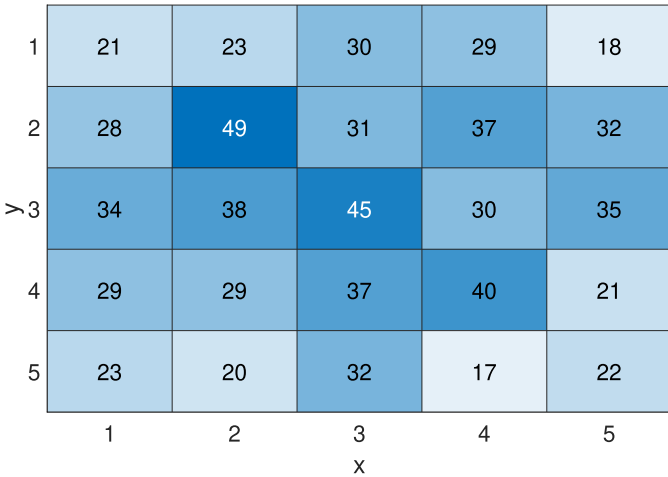(c) Heatmap of UEs on the user plane for bs_{20_3}, bs_{20_4}, and bs_{20_5}.

Fig. 8. Locations of $bs20\_3$ found by the CGA with $m\_ue_{5\_5}$, $bs20\_4$ found by the M_CGA with $m\_ue_{5\_10}$, and $bs20\_5$ found by the EM_CGA with $em\_ue_{5\_5}$ with corresponding heatmaps of BSs on the walls and UEs on the user plane (with the ideal scenario).

produce the three deployments) on the user plane are provided in Fig. 9b, showing that they are almost equally distributed.

In summary, the experiments in this section support the expectation that there might be an optimized M BS deployment for K mobile UEs in the confined environment, and
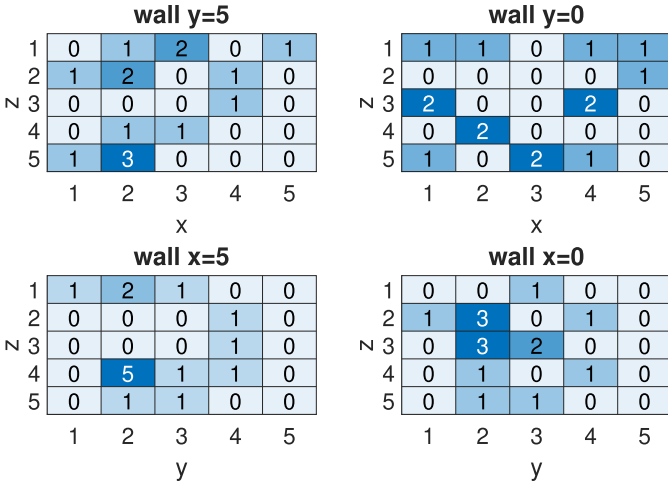
(a) Heatmap of BSs on each wall for bs_{20_6n}, bs_{20_7n}, and bs_{20_8n}.

(b) Heatmap of UEs on the user plane for bs_{20_6n}, bs_{20_7n}, and bs_{20_8n}.

Fig. 9. Heatmap of BSs on each wall and UEs on the user plane for bs_{20_6n}, bs_{20_7n}, and bs_{20_8n}. Each BS deployment is proposed by EM_CGA with $em\_ue_{5\_5}$ (with the non-ideal scenario).
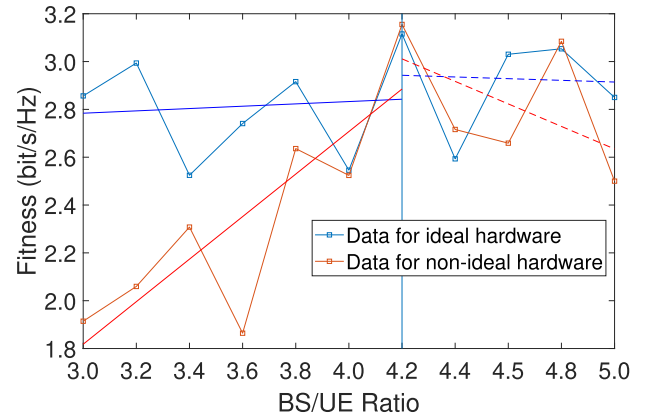

Fig. 10. Focusing performances of BS deployments with different BS/UE ratios (and the linear regression fit curves before and after the best BS/UE ration 4.2) under the ideal and non-ideal hardware conditions.
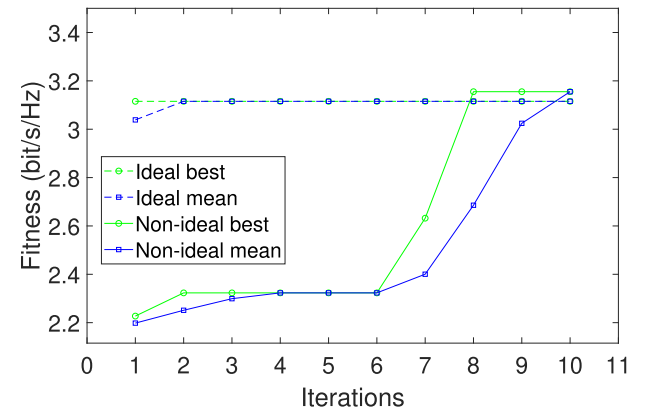

Fig. 11. Search trend of EM_CGA with BS/UE ratio as 4.2 ($K = 5$, $M = 21$).

such deployment is not related to the UE locations. Also, the proposed algorithm (M_CGA and EM_CGA belong to the big class of CGA) is able to find that topology in both ideal and non-ideal scenarios.

D. Simulation Mimicking the Reality

The previous experiments do not ideally approach the real BS deployment problem: although the number of UEs K can be estimated before an event, the required number of BSs M for those UEs is unknown. Neither there is evidence that the equally distributed BS on the walls could improve the system performance. Therefore, we do not hold such symmetrical assumption in the experiments mimicking the reality.

The encoding of the CGA is adapted for this experiment. The length of the binary matrix L is expanded with 2 bits representing the relative position on the walls (e.g. [00] for wall $x = 0$, [01] for wall $y = 0$). A population is still an array containing P instances of L but the fixed order mapping to walls is not used. The crossover and mutation operations

can change the encoded location of a BS to different walls. In realistic applications, the ratio of the BS numbers to the UE numbers (BS/UE ratio) is more meaningful than the absolute values for the scalability. The number of BSs M is changed to a range $[15, 25]$, while the number of UEs K and other parameter settings remain same. Therefore the BS/UE ratio is in the range $[3, 5]$. The EM_CGA is applied to tackle this problem with both the ideal and the non-ideal scenarios.

Figure 10 summarizes the focusing performances of different BSs deployments with variant BS/UE ratios. The best average focusing performance for $K = 5$ mobile UEs is achieved with the BS/UE ratio of 4.2 ($M = 21$) for both scenarios (3.12 bit/s/Hz for the ideal scenario and 3.16 bit/s/Hz for the non-ideal scenario). Since the data points are near-optimal values found by the algorithm, small fluctuating behavior is reasonable and we focus on the trend. The linear regression fit (in a least-squares sense) curves are also provided in Figure 10: the focusing performance is enhancing when the BS/UE ratio is increasing since each UE is served with more BSs. However, in both scenarios if the BS/UE ratio is relatively large (larger than 4.2), the focusing performance can not continue to improve when more BSs are deployed.

The search trends of the EM_CGA for the BS/UE ratio as 4.2 ($k = 5$, $M = 21$) under both scenarios are presented in Fig. 11. Over iterations the algorithm finds candidates with better average performance (with an increasing mean curve).

The candidate with the best average performance in the final generation is proposed as the solution. For the ideal scenario, the algorithm stays converged since iteration 2. For the non-ideal scenario, the algorithm starts from candidates with low average performances but finally reaches candidates with good performances.

In summary, the simulations in this section demonstrate the general applicability of our proposed algorithm for an optimized solution to the BS deployment problem in both ideal and non-ideal scenarios.

V. Conclusion

This paper proposed a customized genetic algorithm combined with ray tracer channel simulator for optimizing the cell-free mMIMO topology for multiple users. The novelty of the algorithm is the special design of the warm-start strategy, the selection policy, and the elitism stage, which help to find better candidate solutions with a faster convergence speed in the simulations. The mMIMO system model incorporates the effect of hardware impairment in practice, and the non-ideal BSs/UEs are formulated for the focusing performance.

Simulation experiments with both ideal and non-ideal hardwares have been performed for indoor scenarios of a fixed number of BSs serving multiple static and mobile UEs, as well as an unknown number of BSs mimicking real topology optimization problems. The simulation results indicate that there exists an optimized placement of BSs not correlated with the UEs positions in the confined indoor environment. In the near-optimal BS deployment solution proposed by our algorithm, on each wall of the room the BSs are not evenly distributed, which is very interesting. It is also observed that the best ratio between the number of BSs and the number of UEs is 4.2, above which the focusing performance does not increase any more. Moreover, the deployment result for the non-ideal hardware differs from that of the ideal hardware, indicating that we have to take into account the hardware/device quality for the topology optimization in practice.

As an exciting future development of this work, we will investigate the premature convergence issue in the applications of GA turning near-optimal to optimal solutions for cell-free mMIMO. We will also investigate the more general applicable approach requiring as fewer problem specific characteristics as possible.

References

[1] A. Bourdoux *et al.*, "6G white paper on localization and sensing," 2020, *arXiv:2006.01779*.

[2] C. De Lima *et al.*, "Convergent communication, sensing and localization in 6G systems: An overview of technologies, opportunities and challenges," *IEEE Access*, vol. 9, pp. 26902–26925, 2021, doi: 10.1109/ACCESS.2021.3053486.

[3] E. Björnson, E. G. Larsson, and T. L. Marzetta, "Massive MIMO: Ten myths and one critical question," *IEEE Commun. Mag.*, vol. 54, no. 2, pp. 114–123, Feb. 2016.

[4] K. Shen, T. De Pessemier, L. Martens, W. Joseph, and Y. Miao, "Genetic algorithm combined with ray tracer for optimizing cell-free mMIMO topology in a confined environment," in *Proc. 15th Eur. Conf. Antennas Propag. (EuCAP)*, Mar. 2021, pp. 1–5, doi: 10.23919/EuCAP51087.2021.9410934.

[5] E. Björnson, L. Sanguinetti, H. Wymeersch, J. Hoydis, and T. L. Marzetta, "Massive MIMO is a reality—What is next?: Five promising research directions for antenna arrays," 2019, *arXiv:1902.07678*.

[6] H. Q. Ngo, A. Ashikhmin, H. Yang, E. G. Larsson, and T. L. Marzetta, "Cell-free massive MIMO versus small cells," *IEEE Trans. Wireless Commun.*, vol. 16, no. 3, pp. 1834–1850, Jan. 2017.

[7] C. Qin, Y. Miao, Y. Gao, J. Chen, J. Zhang, and A. A. Glazunov, "Simulation-based investigation on spatial channel hardening of massive MIMO in different indoor scenarios and with different array topologies," in *Proc. XXXIIIrd Gen. Assem. Sci. Symp. Int. Union Radio Sci.*, Aug. 2020, pp. 1–4, doi: 10.23919/URSIGASS49373.2020.9232421.

[8] Y. Miao, S. Pollin, and A. A. Glazunov, "Simulation-based investigation on massive multi-antenna system as to spatial channel hardening for mobile single user in a controlled multipath environment," in *Proc. 14th Eur. Conf. Antennas Propag. (EuCAP)*, Copenhagen, Denmark, Mar. 2020, pp. 1–5, doi: 10.23919/EuCAP48036.2020.9135757.

[9] D. A. Schmidt, M. Joham, and W. Utschick, "Minimum mean square error vector precoding," in *Proc. IEEE 16th Int. Symp. Pers., Indoor Mobile Radio Commun.*, Apr. 2005, pp. 107–111, doi: 10.1109/PIMRC.2005.1651408.

[10] F. Mani, "Improved ray-tracing for advanced radio propagation channel modeling," Ph.D. dissertation, Univ. Catholique de Louvain, Ottignies-Louvain-la-Neuve, Belgium, Jun. 2012.

[11] F. Mani, F. Quitin, and C. Oestges, "Directional spreads of dense multipath components in indoor environments: Experimental validation of a ray-tracing approach," *IEEE Trans. Antennas Propag.*, vol. 60, no. 7, pp. 3389–3396, Jul. 2012, doi: 10.1109/TAP.2012.2196942.

[12] Y. Miao, T. Pedersen, M. Gan, E. Vinogradov, and C. Oestges, "Reverberant room-to-room radio channel prediction by using rays and graphs," *IEEE Trans. Antennas Propag.*, vol. 67, no. 1, pp. 484–494, Jan. 2019.

[13] K. Haneda *et al.*, "Radio propagation modeling methods and tools," in *Inclusive Radio Communications 5G Beyond*, C. Oestges, F. Quitin, Eds. New York, NY, USA: Academic, 2021, ch. 2, pp. 7–48, doi: 10.1016/B978-0-12-820581-5.00008-0.

[14] Y. Miao, Q. Gueuning, M. Gan, and C. Oestges, "Adding diffuse scattering correlation to effective roughness models in ray tracing," in *Proc. 11th Eur. Conf. Antennas Propag. (EUCAP)*, Paris, France, Mar. 2017, pp. 828–830.

[15] Y. Miao, Q. Gueuning, and C. Oestges, "Modeling the phase correlation of effective diffuse scattering from surfaces for radio propagation prediction with antennas at refined separation," *IEEE Trans. Antennas Propag.*, vol. 66, no. 3, pp. 1427–1435, Mar. 2018.

[16] D. Whitley, "A genetic algorithm tutorial," *Statist. Comput.*, vol. 4, no. 2, pp. 65–85, Jun. 1994.

[17] M. O. Binelo, A. L. F. D. Almeida, and F. R. P. Cavalcanti, "MIMO array capacity optimization using a genetic algorithm," *IEEE Trans. Veh. Technol.*, vol. 60, no. 6, pp. 2471–2481, Jul. 2011.

[18] P. Uthansakul, D. Assanuk, and M. Uthansakul, "The use of genetic algorithm for designing MIMO antenna placement," in *Proc. Int. Conf. Comput. Inf. Appl.*, Tianjin, China, Dec. 2010, pp. 414–417.

[19] B. Makki, A. Ide, T. Svensson, T. Eriksson, and M.-S. Alouini, "A genetic algorithm-based antenna selection approach for large-but-finite MIMO networks," *IEEE Trans. Veh. Technol.*, vol. 66, no. 7, pp. 6591–6595, Jul. 2017.

[20] N. Sharma and K. R. Anupama, "A novel genetic algorithm for adaptive resource allocation in MIMO-OFDM systems with proportional rate constraint," *Wireless Pers. Commun.*, vol. 61, no. 1, pp. 113–128, Jan. 2011.

[21] X. Ma, F. Yang, S. Liu, J. Song, and Z. Han, "Design and optimization on training sequence for mmWave communications: A new approach for sparse channel estimation in massive MIMO," *IEEE J. Sel. Areas Commun.*, vol. 35, no. 7, pp. 1486–1497, Jul. 2017.

[22] S. K. Goudos, P. D. Diamantoulakis, and G. K. Karagiannidis, "Multi-objective optimization in 5G wireless networks with massive MIMO," *IEEE Commun. Lett.*, vol. 22, no. 11, pp. 2346–2349, Nov. 2018.

[23] I. V. Rao and V. M. Rao, "Optimal transmit antenna selection using improved GSA in massive MIMO technology," *Wireless Pers. Commun.*, vol. 109, pp. 1217–1235, May 2019.

[24] E. Björnson, J. Hoydis, M. Kountouris, and M. Debbah, "Massive MIMO systems with non-ideal hardware: Energy efficiency, estimation, and capacity limits," *IEEE Trans. Inf. Theory*, vol. 60, no. 11, pp. 7112–7139, Nov. 2014.

[25] C. Studer, M. Wenk, and A. Burg, "MIMO transmission with residual transmit-RF impairments," in *Proc. Int. ITG Workshop Smart Antennas (WSA)*, Feb. 2010, pp. 189–196.

[26] E. Björnson, J. Hoydis, and L. Sanguinetti, "Massive MIMO networks: Spectral, energy, and hardware efficiency," *Found. Trends Signal Process.*, vol. 11, nos. 3–4, pp. 154–655, 2017, doi: 10.1561/2000000093.

[27] O. T. Demir and E. Bjornson, "The Bussgang decomposition of nonlinear systems: Basic theory and MIMO extensions [lecture notes]," *IEEE Signal Process. Mag.*, vol. 38, no. 1, pp. 131–136, Jan. 2021.

[28] J. Zhang, Y. Wei, E. Bjornson, Y. Han, and S. Jin, "Performance analysis and power control of cell-free massive MIMO systems with hardware impairments," *IEEE Access*, vol. 6, pp. 55302–55314, 2018.

[29] J. Zheng, J. Zhang, L. Zhang, X. Zhang, and B. Ai, "Efficient receiver design for uplink cell-free massive MIMO with hardware impairments," *IEEE Trans. Veh. Technol.*, vol. 69, no. 4, pp. 4537–4541, Apr. 2020.

[30] S. Elhoushy and W. Hamouda, "Performance of distributed massive MIMO and small-cell systems under hardware and channel impairments," *IEEE Trans. Veh. Technol.*, vol. 69, no. 8, pp. 8627–8642, Aug. 2020.

[31] H. Masoumi and M. J. Emadi, "Performance analysis of cell-free massive MIMO system with limited fronthaul capacity and hardware impairments," *IEEE Trans. Wireless Commun.*, vol. 19, no. 2, pp. 1038–1053, Feb. 2020.

[32] L. Xu, X. Lu, S. Jin, F. Gao, and Y. Zhu, "On the uplink achievable rate of massive MIMO system with low-resolution ADC and RF impairments," *IEEE Commun. Lett.*, vol. 23, no. 3, pp. 502–505, Mar. 2019.

[33] X. Zhang, D. Guo, K. An, and B. Zhang, "Secure communications over cell-free massive MIMO networks with hardware impairments," *IEEE Syst. J.*, vol. 14, no. 2, pp. 1909–1920, Jun. 2020.

[34] A. O. Martinez, E. D. Carvalho, and J. O. Nielsen, "Massive MIMO properties based on measured channels: Channel hardening, user decorrelation and channel sparsity," in *Proc. 50th Asilomar Conf. Signals, Syst. Comput.*, Pacific Grove, CA, USA, Nov. 2016, pp. 1804–1808.

[35] *5G, NR, Base Station (BS) Radio Transmission and Reception*, 3GPP Tech. Specifications, document TS 38.104, V 15.3.0 (Rel 15), 2018.

[36] Y. Zhang, M. Zhou, Y. Cheng, L. Yang, and H. Zhu, "RF impairments and low-resolution ADCs for nonideal uplink cell-free massive MIMO systems," *IEEE Syst. J.*, vol. 15, no. 2, pp. 2519–2530, Jun. 2021.

[37] M. E. Leinonen, M. Jokinen, N. Tervo, O. Kursu, and A. Parssinen, "System EVM characterization and coverage area estimation of 5G directive mmW links," *IEEE Trans. Microw. Theory Techn.*, vol. 67, no. 12, pp. 5282–5295, Dec. 2019.

[38] M.-Y. Huang, T. Chi, S. Li, T.-Y. Huang, and H. Wang, "A 24.5–43.5-GHz ultra-compact CMOS receiver front end with calibration-free instantaneous full-band image rejection for multiband 5G massive MIMO," *IEEE J. Solid-State Circuits*, vol. 55, no. 5, pp. 1177–1186, May 2020.

[39] H. T. Nguyen, T. Chi, S. Li, and H. Wang, "A linear high-efficiency millimeter-wave CMOS Doherty radiator leveraging multi-feed on-antenna active load modulation," *IEEE J. Solid-State Circuits*, vol. 53, no. 12, pp. 3587–3598, Dec. 2018.

[40] P. Rodríguez-Vázquez, J. Grzyb, B. Heinemann, and U. R. Pfeiffer, "A 16-QAM 100-Gb/s 1-M wireless link with an EVM of 17% at 230 GHz in an SiGe technology," *IEEE Microw. Wireless Compon. Lett.*, vol. 29, no. 4, pp. 297–299, Apr. 2019.

[41] B. Yang, Z. Yu, J. Lan, R. Zhang, J. Zhou, and W. Hong, "Digital beamforming-based massive MIMO transceiver for 5G millimeter-wave communications," *IEEE Trans. Microw. Theory Techn.*, vol. 66, no. 7, pp. 3403–3418, Jul. 2018.

[42] C. F. Lima, M. Pelikan, D. E. Goldberg, F. G. Lobo, K. Sastry, and M. Hauschild, "Influence of selection and replacement strategies on linkage learning in BOA," in *Proc. IEEE Congr. Evol. Comput.*, Singapore, Sep. 2007, pp. 1083–1090.

[43] C. E. Andrade, T. Silva, and L. S. Pessoa, "Minimizing flowtime in a flowshop scheduling problem with a biased random-key genetic algorithm," *Expert Syst. Appl.*, vol. 128, pp. 67–80, Aug. 2019.

[44] A. Lipowski and D. Lipowska, "Roulette-wheel selection via stochastic acceptance," *Phys. A, Statist. Mech. Appl.*, vol. 391, no. 6, pp. 2193–2196, 2012.

[45] O. Hasançebi and F. Erbatur, "Evaluation of crossover techniques in genetic algorithm based optimum structural design," *Comput. Struct.*, vol. 78, nos. 1–3, pp. 435–448, Nov. 2000.

[46] F. Ye, C. Doerr, and T. Bäck, "Interpolating local and global search by controlling the variance of standard bit mutation," in *Proc. IEEE Congr. Evol. Comput. (CEC)*, Wellington, New Zealand, Jun. 2019, pp. 2292–2299.

[47] I. Harvey, "The microbial genetic algorithm," in *Proc. Eur. Conf. Artif. Life*, Berlin, Germany, Sep. 2009, pp. 126–133.

[48] H. Du, Z. Wang, W. Zhan, and J. Guo, "Elitism and distance strategy for selection of evolutionary algorithms," *IEEE Access*, vol. 6, pp. 44531–44541, 2018.

[49] C. W. Ahn and R. S. Ramakrishna, "Elitism-based compact genetic algorithms," *IEEE Trans. Evol. Comput.*, vol. 7, no. 4, pp. 367–385, Aug. 2003.

[50] C. A. Hoare, "Quicksort," *Comput. J.*, vol. 5, no. 1, pp. 10–16, 1962.

[51] *Effects of Building Materials and Structures on Radiowave Propagation Above About 100 MHz International Telecommunication Union—Radiocommunication Sector (ITU-R)*, document 2040-1, P-Series Radiowave Propagation, Jul. 2015.

[52] K. Shen, T. De Pessemier, X. Gong, L. Martens, and W. Joseph, "Genetic optimization of energy-and failure-aware continuous production scheduling in pasta manufacturing," *Sensors*, vol. 19, no. 297, p. 297, Jan. 2019.

[53] R. V. Lenth, "Some practical guidelines for effective sample size determination," *Amer. Statistician*, vol. 55, no. 3, pp. 87–193, 2001.

[54] H. Abdi and P. Molin, "Lilliefors/Van Soest's test of normality," in *Encyclopedia of Measurement and Statistics*. New York, NY, USA: SAGE, 2007, pp. 540–544.

[55] S. C. Abrahams and E. T. Keve, "Normal probability plot analysis of error in measured and derived quantities and standard deviations," *Acta Crystallographica Sect. A, Crystal Phys., Diffraction, Theor. Gen. Crystallogr.*, vol. 27, no. 2, pp. 157–165, Mar. 1971.

Ke Shen received the B.Eng. degree in software engineering from Xidian University, Xi'an, China, in 2015, the M.E. degree (Diplôme D'ingénieur) from the École Nationale Supérieure d'Informatique pour l'Industrie et l'Entreprise (National School of Computer Science for Industry and Business), France, in 2017, and the M.Sc. degree from Université Paris-Saclay (Paris-Saclay University), France, in 2017. He is currently pursuing the Ph.D. degree with Ghent University, Belgium. His research interests are evolutionary computation, production scheduling, operations research, and artificial intelligence.

Siavash Safapourhajari (Member, IEEE) was born in Bandaranzali, Iran, in 1987. He received the B.Sc. and M.Sc. degrees in electrical engineering from the University of Tehran, Tehran, Iran, and the Ph.D. degree from the Faculty of Electrical Engineering, Computer Science and Mathematics (EEMCS), University of Twente, The Netherlands, in 2015, where he focused on ultra-narrowband communications for low power Internet of Things (IoT). His research interests include signal processing for communications, efficient implementation of signal processing algorithms, low power IoT, and antenna arrays. He was a recipient of the German Academic Exchange Service (DAAD) Fellowship for Research Project with the University of Rostock, during his M.Sc. study.

Toon De Pessemier received the M.Sc. degree in computer science engineering from Ghent University in 2006 and the Ph.D. degree in 2013, on his research "improved online services by personalized recommendations and optimal quality of experience parameters." In 2015, he obtained a Post-Doctoral Scholarship for his research "Design and validation of innovative techniques to assist people in the decision making process by analyzing data of user behavior and contextual features." Since 2018, he has been a part-time Professor and teaches a Recommender Systems. His another research topic that, he investigates is scheduling of production environments.

Luc Martens (Member, IEEE) received the M.Sc. degree in electrical engineering from Ghent University, Ghent, Belgium, in July 1986. From September 1986 to December 1990, he was a Research Assistant with the Department of Information Technology (INTEC), Ghent University. During this period, his scientific work was focused on the physical aspects of hyperthermic cancer therapy. His research work dealt with electromagnetic and thermal modeling and with the development of measurement systems for that application. This work led to the Ph.D. degree in December 1990. Since 1991, he has been manages the WAVES Research Group, INTEC. Since 2004, this group is a part of the iMinds Institute and since April 1993, he has been a Professor with Ghent University. He is the author or coauthor of more than 300 publications in the domain of electromagnetic channel predictions, dosimetry, exposure systems, and health and wireless communications. His experience and current research interests include modeling and measurement of electromagnetic channels, of electromagnetic exposure, such as around telecommunication networks and systems, such as cellular base station antennas and of energy consumption in wireless networks.

Yang Miao (Member, IEEE) received the M.Sc. and Ph.D. degrees from the Radio Propagation Laboratory, Mobile Communications Research Group, Tokyo Institute of Technology, Japan, in 2012 and 2015, respectively. From 2010 to 2015, she was a Research Assistant with the Takada Laboratory, Tokyo Institute of Technology. From 2015 to 2018, she was a Post-Doctoral Researcher with the Institute of Information and Communication Technologies, Electronics, and Applied Mathematics, Universite Catholique de Louvain, Louvain-la-Neuve, Belgium, and IMEC, Wireless, Acoustics, Environment, and the Expert Systems Laboratory, Ghent University, Ghent, Belgium. From 2017 to 2018, she was a part-time Senior Antenna Engineer with Jaguar Radio Wave Corporation, Shenzhen, China. From 2018 to 2019, she was a Research Assistant Professor with the Southern University of Science and Technology, Shenzhen. Since August 2019, she has been an Assistant Professor with the Radio Systems Group, University of Twente, The Netherlands. Since November 2021, she has been also affiliated in part-time with KULeuven as a Marie Curie Individual Fellow. Her current research focuses on joint communication and sensing, incorporating mobility, and human factors.

Wout Joseph (Senior Member, IEEE) was born in Ostend, Belgium, in October 1977. He received the M.Sc. degree in electrical engineering from Ghent University, Belgium, in July 2000, and the Ph.D. degree in March 2005, this work dealt with measuring and modeling of electromagnetic fields around base stations for mobile communications related to the health effects of the exposure to electromagnetic radiation. From 2007 to 2012, he was a Post-Doctoral Fellow of the FWO-V (Research Foundation—Flanders). Since October 2009, he has been a Professor in the domain of "Experimental Characterization of Wireless Communication Systems." He has been an IMEC PI since 2017. His professional interests are electromagnetic field exposure assessment, propagation for wireless communication systems, antennas, and calibration. Furthermore, he specializes in wireless performance analysis and quality of experience.